Journal of Instrumentation

# A study of astrometric distortions due to "tree rings" in CCD sensors using LSST Photon Simulator

PUBLISHED BY IOP PUBLISHING FOR SISSA MEDIALAB

RECEIVED: *February 18, 2015*
ACCEPTED: *February 28, 2015*
PUBLISHED: *May 22, 2015*

PRECISION ASTRONOMY WITH FULLY DEPLETED CCDS
4–5 DECEMBER 2014
BROOKHAVEN NATIONAL LABORATORY, U.S.A.



# A study of astrometric distortions due to "tree rings" in CCD sensors using LSST Photon Simulator

**B. Beamer**[a,1] **A. Nomerotski**[b] **and D. Tsybychev**[a]

[a]*Department of Physics and Astronomy, Stony Brook University, Stony Brook NY, 11794, U.S.A.*
[b]*Department of Physics, Brookhaven National Laboratory, Bldg. 510, Upton NY, 11973, U.S.A.*

*E-mail:* benjamin.beamer@stonybrook.edu

ABSTRACT: Imperfections in the production process of thick CCDs lead to circularly symmetric dopant concentration variations, which in turn produce electric fields transverse to the surface of the fully depleted CCD that displace the photogenerated charges. We use PhoSim, a Monte Carlo photon simulator, to explore and examine the likely impacts these dopant concentration variations will have on astrometric measurements in LSST. The scale and behavior of both the astrometric shifts imparted to point sources and the intensity variations in flat field images that result from these doping imperfections are similar to those previously observed in Dark Energy Camera CCDs, giving initial confirmation of PhoSim's model for these effects. Additionally, organized shape distortions were observed as a result of the symmetric nature of these dopant variations, causing nominally round sources to be imparted with a measurable ellipticity either aligned with or transverse to the radial direction of this dopant variation pattern.

KEYWORDS: Systematic effects; Detectors for UV, visible and IR photons

[1]Corresponding author.



doi:10.1088/1748-0221/10/05/C05027

## Contents



## 1 Large Synoptic Survey Telescope (LSST)

The Large Synoptic Survey Telescope (LSST) is a next generation telescope designed to provide a 6-band (ugrizy) survey of 20,000 square degrees of the Southern sky over its 10-year mission, beginning in 2022. This survey is intended to measure the positions and shapes of billions of galaxies to investigate Dark Energy and Dark Matter through weak lensing effects, however, due to the unprecedented breadth (and depth) of the survey, it will also serve to map numerous astronomical objects, both within our solar system and throughout the Milky Way, as well as to detect a variety of transient astronomical phenomena [1].

For the LSST, a unique, 3.1 gigapixel camera has been designed. The focal plane will consist of 189 4k by 4k CCDs and give a 9.6 square degree field of view. These CCDs are 100 $\mu$m thick with p-type fully depleted silicon and n-type buried channel; and have a pixel size of 10 $\mu$m [1].

### 1.1 PhoSim: LSST Photon Simulator

In order to address as many systematic issues as possible prior to the completion of the LSST and camera themselves, a code package called "the Photon Simulator" (PhoSim) was developed to do Monte Carlo simulations of astronomical images. PhoSim works by propagating individual photons through the atmosphere, telescope, and camera to produce a final, pixelated image [2]. Models for a wide variety of systematic-inducing phenomena (from atmospheric effects to optics to sensor effects) are included so that the final image is as close as possible to what would actually be seen by the physical telescope. Simulated sensor effects include charge diffusion, wavelength-dependent



2015 JINST 10 C05027

photon penetration, pixel saturation, blooming, imperfect pixel boundaries, the brighter-fatter effect (further discussion in ref. [3]), and others in addition to the dopant concentration variations of interest to this investigation.

### 1.2 "Tree rings" and astrometry

"Tree rings", as they have come to be known, originate from variations in the dopant concentration during the growth of the single-crystal silicon boule. These dopant variations are radially symmetric about the center of the silicon boule, and give rise to small lateral electric fields due to the resulting space-charge gradient [4]. These fields cause the electrons to shift laterally as they traverse the chip from the point of photon conversion to the gates at the back of the chip, altering the position at which the electron eventually registers relative to an ideal, perfectly homogenously doped silicon sensor. While this deviation is typically quite small, it results in systematic biases in the measured position of objects based on the location at which they are observed on the CCD, and needs to be corrected for.

Further, as there is nominally only a charge gradient in the radial direction, these electric fields also distort the shapes of observed objects, causing stretching or compression along the radial axis while leaving the perpendicular axis undisturbed. This introduces a measurable ellipticity to point sources and, if left uncorrected, may bias shear measurements and corresponding weak lensing results. The goal of this study is to verify that PhoSim's model reproduces similar effects to those seen in currently existing telescopes and to explore the less-apparent impacts of such sensor imperfections in a controlled environment.

## 2 Simulation analysis

To isolate the impact these dopant variations have on astrometric results, these simulations were done using an idealized instrument setup within PhoSim which removes all atmospheric, optical, and alignment-based disturbances to the photon path, isolating the sensor-based distortions of interest to this investigation. A range of dopant concentration variations were used to explore the dependence of the various distortions on the severity of these dopant variations. All simulations were done with a dopant variation period of 100 pixels. Two different varieties of object fields were considered; fields of numerous identical monochromatic point sources and fields with completely even monochromatic light over the entire focal plane ("flats"). Each requires similar but distinct analysis techniques.

### 2.1 Object fields

The "object fields" consisted of either regular grids of identical monochromatic point sources ("stars") or identical monochromatic point sources randomly scattered across the central CCD such that there was no object overlap. Simulations were done with a range of degrees of dopant variations using the same randomized object field, and SExtractor [5] was used to identify the centroid position in sensor coordinates (X_IMAGE and Y_IMAGE) and relevant ellipticity parameters (the second moments, CXX_ IMAGE, CYY_ IMAGE, and CXY_IMAGE and major and minor axis RMS values, A_IMAGE and B_IMAGE) of each object. These positions were then compared against the location of the same object in a control simulation with an ideal chip without dopant variations to map the distortion in observed position with respect to the ideal object position over the CCD.

### 2.2 Flat field exposures

The flat fields consisted of an empty object field with an even distribution of incident monochromatic light. Similarly to the point source simulations, a range of dopant variations was simulated to explore the impact and relation between the degree of dopant variation and the variation in detected flux. Pixel flux values were binned by distance from the center of the silicon boule and averaged to produce profiles of measured pixel flux as a function of radius.

## 3 Distortions due to "tree rings"

In PhoSim, "tree ring"-based distortions are modeled as a perfect sinusoidal variation in the dopant concentration as a function of variation amplitude, period, and origin. Fundamentally, all of the following distortions are produced by the radial shifts imparted to electrons as they traverse the bulk of the silicon; in addition, several effects occur which have the same origin as the shifts in measured position of point sources. These include the intensity variations observed in flat field images, shape distortions of objects based on their position relative to the origin of the original silicon boule, and the chromatic dependence of these distortions. An illustration of the relation between the dopant concentration variation (green) and the related effects can be seen in figure 1. As this dopant variation is also an effective variation in space-charge density, they induce lateral electric fields (blue) proportional to this charge gradient. This causes the electrons to be shifted by a distance proportional to the local lateral electric field (represented by the black arrows). Finally, the slight variation in the strength of these fields over the cross-section of the object causes the object's shape to be distorted based on its location within the tree ring pattern, which is illustrated by the ellipses towards the bottom of the image (further detail in section 3.5).

### 3.1 Astrometric shifts

The most readily apparent impact of these dopant variations are the astrometric shifts imparted to objects based on the position at which they are detected on the CCD. As such, this is a natural entry point to confirm that our understanding of the model is accurate and that the model recreates results that are similar to those observed in real-world data.

Figure 2 maps the astrometric shifts experienced by 420 nm point sources as a function of their detection position on the CCD when 5% dopant variations are included in the simulation. In the left image, the shifts are plotted as a function of the position on the CCD at which the object was detected under nominal conditions, with the magnitude and direction of the astrometric shift indicated by the length and direction of the arrow. In the image to the right, these shifts are graphed as a function of the objects radial distance from the origin of the dopant variation pattern, with a positive shift corresponding to a shift away from the origin and a negative shift corresponding to a shift towards the origin. From this, it can readily be seen that these shifts are well represented by a sine function with a 100 pixel period and a shift amplitude of 0.016 pixels. The observed shifts are comparable in scale and behavior to those observed in the DECam [6]. Simulations were done for a range of dopant variation severities, and the astrometric shift patterns were fitted with a sine



2015 JINST 10 C05027

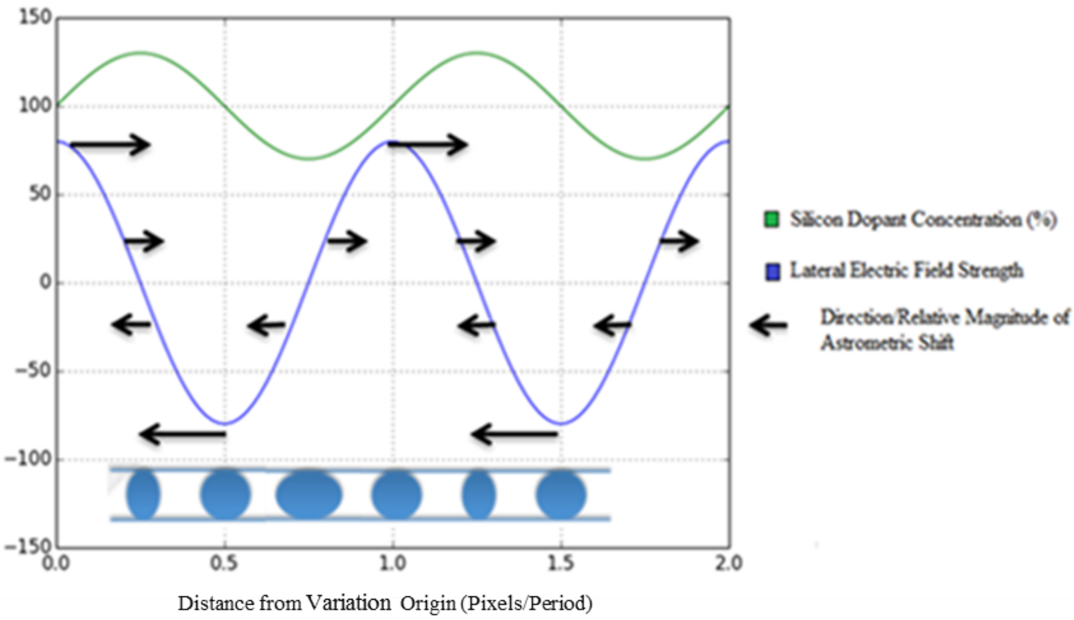


**Figure 1**. Illustration of the relationship between the dopant concentration variation (green), resulting lateral electric fields (blue), approximate scale of the local induced astrometric shifts (black arrows) and shapes of nominally round point sources (blue ellipses).

function using. The amplitudes of the induced astrometric shifts are plotted against the amplitude of the dopant concentration variation for that simulation in figure 3. This relation was expected to be linear as the lateral electric field strength is proportional to the gradient of dopant concentration, which is itself merely the derivative of a sine function in these simulations. As such, increasing the amplitude of the dopant variations should increase the amplitude of the resulting astrometric shifts proportionally, which is precisely what is observed.

### 3.2 Flat field intensity fluctuations

The lateral electric fields responsible for the position deviations seen in point sources similarly distort images taken of flat incident light sources. These fields bias the electrons to travel towards regions with high dopant concentrations and away from regions with low dopant concentrations, resulting in the characteristic tree-ring-like pattern from which this effect draws its name. Figure 4 shows a DS9 [8] image of a simulation of perfectly even incident 420 nm light on a CCD with a dopant variation amplitude of 50%. This closely resembles the effect, albeit more severe by design, observed in flat field images taken by DECam sensors [6]. The right image shows an example of the average intensity profile along the radial direction of the dopant variation for a simulation with a 10% dopant variation, fit with sine and linear functions. As was done for astrometric shifts, a number of simulations were performed with a range of dopant variations, and a graph of the corresponding intensity variations can be seen in figure 5.



2015 JINST 10 C05027

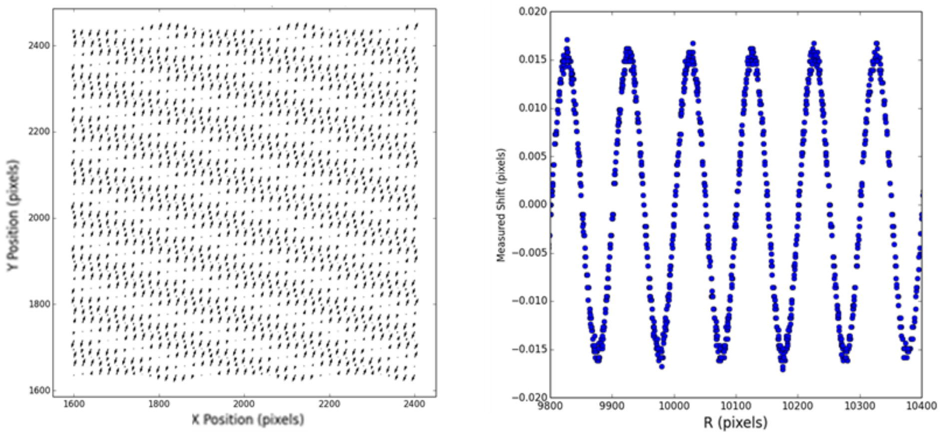


**Figure 2**. (Left) Map showing the direction and magnitude of the astrometric shift experienced by $\sim 1500$ evenly spaced 420 nm point source as a function of nominal position received on the CCD for a dopant concentration variation of 5%. (Right) Astrometric shift as a function of the objects nominal distance from the dopant variation origin.

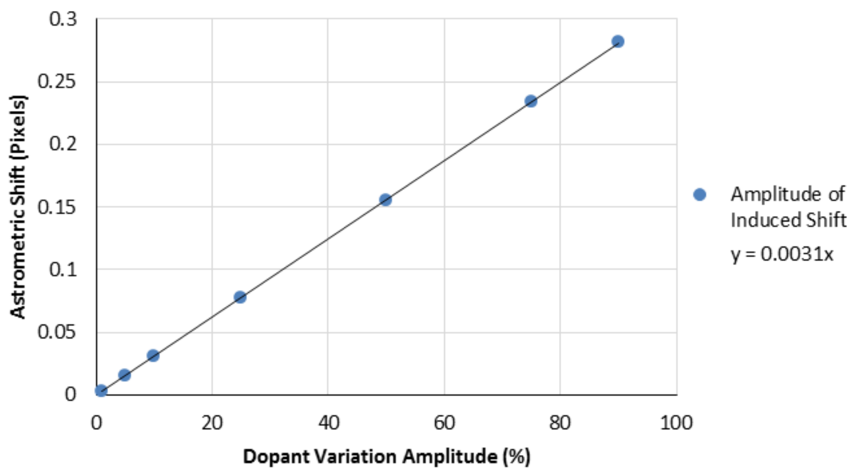


**Figure 3**. Amplitude of the astrometric shifts experienced by 420 nm point sources for a range of dopant concentration variation amplitudes.

### 3.3 Flat field intensity variations and astrometric shift agreement

As the flat field intensity oscillations and object field astrometric shifts are both believed to result from the same physics, the magnitudes of the two effects should be linked in a definite way, shown in the illustration to the left in in figure 6 for the particular case of sine wave implemented in these simulations (general case discussed in [7]). The initial distribution of electrons is flat (top), but the lateral shifts imparted as they traverse the silicon results in the observed variations in the number of detected electrons. As these shifts should not impact the total number of electrons, only the position at which each electron is detected, the total number of electrons shifted out of region A (blue) must be equal to the number of electrons shifted into region B (yellow). This gives the following relation

2015 JINST 10 C05027

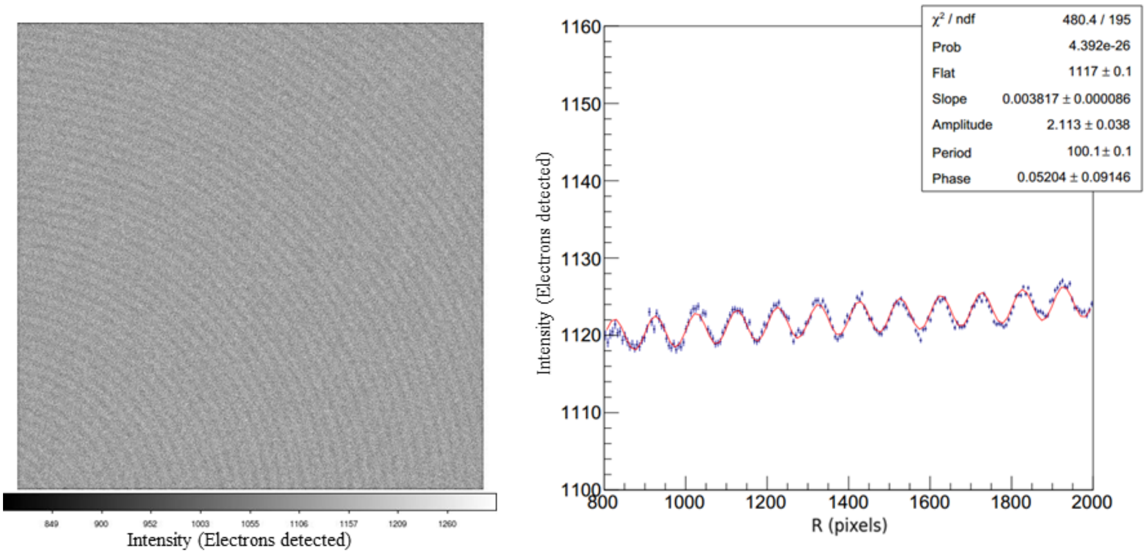


**Figure 4**. (Left) DS9 image of 420 nm flat-field simulation with 50% dopant variation amplitude. The visible waves in the "flat" image correspond to a ∼1% variation in measured intensity. (Right) Average flux received per pixel as a function of pixel distance (R) from the origin of the dopant variations for a 10% variation in dopant concentration (blue points). Curve (red) represents the sine and linear function fit.

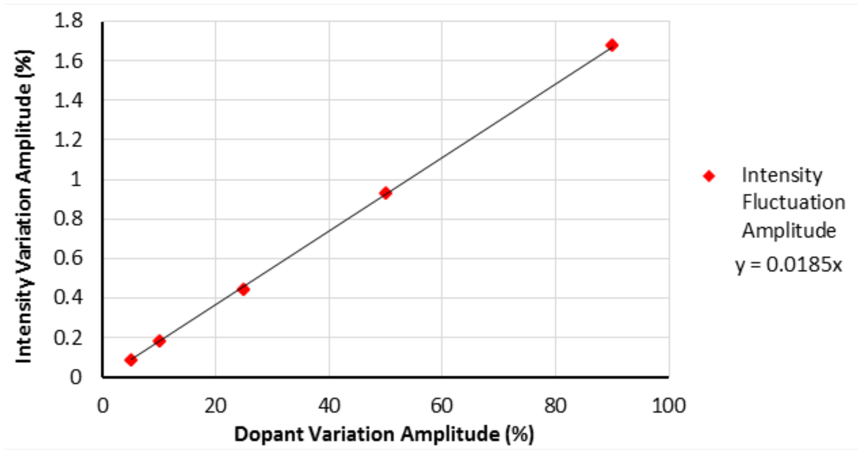


**Figure 5**. Amplitude of the measured intensity fluctuations in monochromatic 420 nm flat-field simulations for a range of dopant concentration variation amplitudes.

between the amplitude of the underlying electron shifts ($\Delta x_{\mathrm{FF}}$) and the amplitude of the observed flux variations ($\Delta I_{FF}$):

$$\Delta x_{\mathrm{FF}} = \left(\frac{\mathrm{Period}}{2\pi}\right) \times \left(\frac{\Delta I_{FF}}{\langle I \rangle}\right).$$

As can be seen in the graph on the right in figure 6, the astrometric shifts directly measured for point sources ($\Delta x_{\mathrm{PS}}$) and the electron shifts inferred from the amplitude of the flat field intensity variations ($\Delta x_{\mathrm{FF}}$) are in close agreement and exhibit the same dependency on dopant concentration variation. The remaining systematic discrepancy of about 5% is under investigation.

2015 JINST 10 C05027

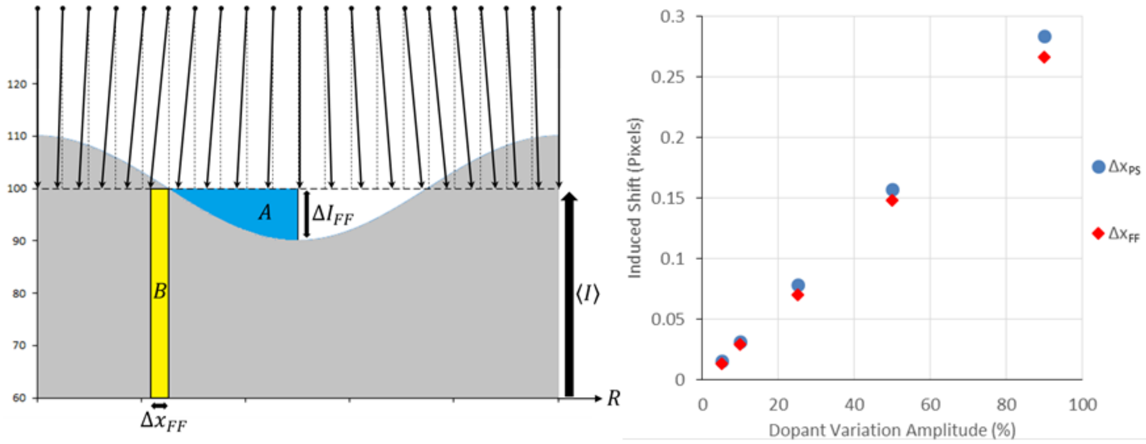


**Figure 6**. (Left) Illustration of the relationship between the amplitude of intensity variations and the amplitude of the underlying electron shifts where the observed intensity variations result from electrons being shifted according to a sine function with amplitude $\Delta x_{\text{FF}}$. (Right) Comparison of the magnitude of directly measured astrometric shifts seen in point sources ($\Delta x_{\text{FF}}$) and the amplitude of the electron shifts required to produce the observed intensity fluctuations in flat-field simulations ($\Delta x_{\text{FF}}$).

### 3.4 Chromatic dependence

All of the aforementioned affects are expected to depend on the wavelength of the incident photon. This is due to the fact that shorter wavelength photons cannot penetrate deeply into the bulk silicon, and convert at the very surface of the sensor. As such, the resulting electron must traverse the entire bulk of the CCD, causing it to accumulate a larger displacement from its nominal path than an electron resulting from the conversion of a longer wavelength photon, which can penetrate deeply into the silicon before converting and beginning to experience these lateral electric fields. This can be seen in the magnitude of the astrometric shifts observed in simulations done with a range of wavelengths and dopant variations in figure 7. The shorter wavelength point sources used, 420 and 600 nm, both convert essentially at the surface, penetrating less than one micron into the sensor, and as such the resulting electrons experience virtually identical shifts. The longer wavelengths used, 800 and 950 nm, however, penetrate an appreciable distance (about 15 $\mu$m and 100 $\mu$m respectively, on average) through the sensor before converting, causing them to accumulate significantly less of a lateral shift.

### 3.5 Shape distortions

The lateral electric fields also impact object shape parameters in several ways as a result of the fact that the strength and direction of these fields varies over small enough scales for electrons detected only a few pixels apart to have experienced slightly different lateral fields as they traversed the bulk of the CCD, and thus acquire slightly different displacements. This can cause nominally round objects to be stretched or compressed based on their location within the tree ring pattern, as can be seen in the illustration in figure 1. Because these fields are radially symmetric about the origin of the original boule, they only distort the object along the radial direction of the dopant concentration variations. This induces a measurable ellipticity to the object with two possible orientations, either aligned with the radial direction of the dopant variation pattern or orthogonal

2015 JINST 10 C05027

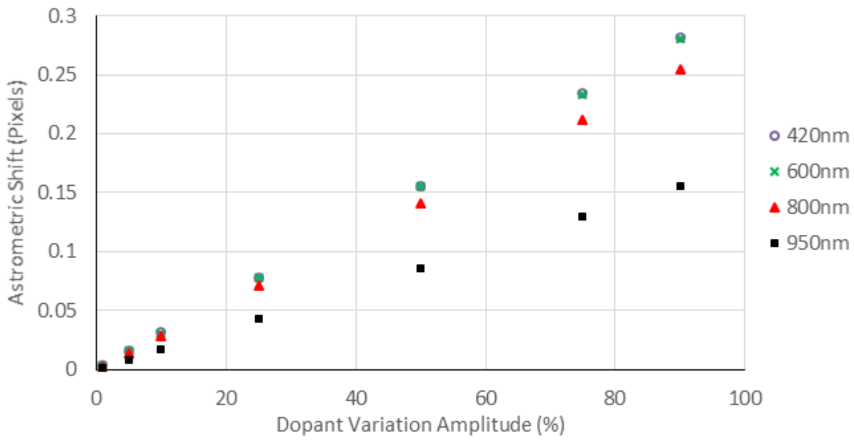


**Figure 7**. Graph showing the amplitude of astrometric shifts experienced by point sources of a range of wavelengths as a function of dopant variation amplitude.

to it, as the radial axis of the object is either stretched longer than the unperturbed orthogonal axis (aligning the ellipse with the radial direction) or compressed to be shorter than the unperturbed axis (aligning the ellipse orthogonal to the radial direction). This behaviour can be seen in figure 8, which shows two graphs detailing the shape distortions imparted by dopant variations. The map to the right shows how the ellipticity varies in both magnitude and orientation across the sensor. The magnitude of the measured ellipticity is represented by the length of the line, and the orientation of the line segment denotes the orientation of the major axis of the ellipse. The expected "flipping" of ellipse orientation can clearly be seen and, when compared with the map of astrometric shifts in figure 2, we also see that the regions in which the ellipses are oriented orthogonally to the radial direction correspond to regions point sources were shifted towards (and the reverse for the regions where the ellipses are oriented parallel to the radial direction). In the graph to the right, we can see how the measured area of the ellipse also varies with the orientation, with the objects that were detected as being larger than the nominal size of ∼3.35 square pixels oriented parallel to the radial direction while the objects detected as smaller than the nominal size are oriented orthogonally to the radial direction. Both of these observations agree with the behaviour predicted of shape distortions caused by dopant concentration variations.

## 4 Conclusions

We used PhoSim to explore the impacts of "tree rings" resulting from a sinusoidal variation in dopant concentration on LSST images to both verify that PhoSim's model reproduces similar effects to those seen in currently existing telescopes, both in terms of scale and behavior, and to explore the less-apparent impacts of such sensor imperfections in a controlled environment. We observed that PhoSim's model for tree-ring-based effects does indeed produce astrometric shifts and flat field intensity variations comparable to those seen in DECam data, and that the magnitudes of these two effects are proportional to one another, as expected. Additionally, we observed that the severity of the observed effects are chromatically dependent, as would be expected simply from the greater ability of longer wavelengths to penetrate into the bulk of the silicon and allowing the resulting electron to circumvent some portion of the lateral electric fields responsible for these



2015 JINST 10 C05027

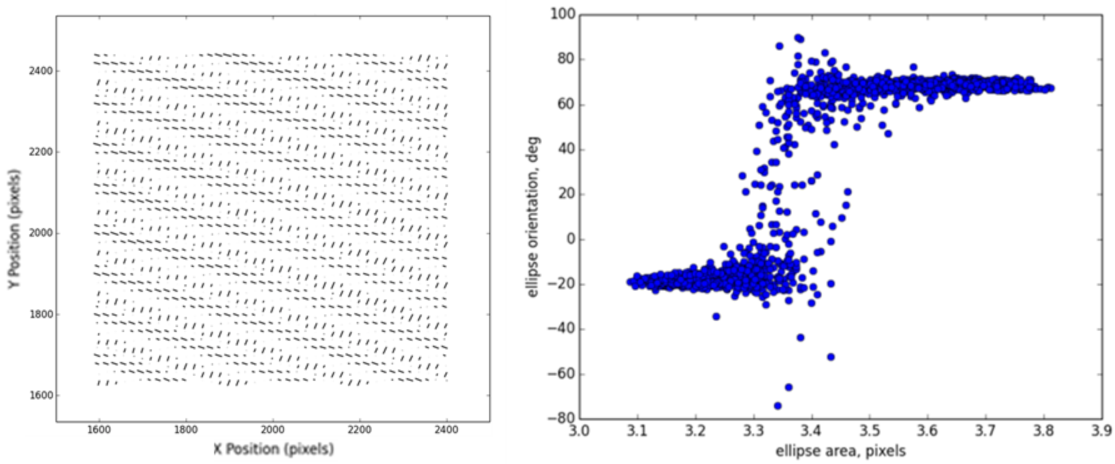


**Figure 8**. (Left) Map of the measured magnitude and orientation of the ellipticity of 420 nm point sources as a function of the nominal position received on the CCD; all sources would be round under ideal conditions. (Right) Object ellipticity orientation compared against object size.

effects. In addition to verifying PhoSim's model for tree-ring-based effects, we also observed induced distortions in the shape of nominally round point sources. These shape distortions impact both the measured ellipticity parameters and object size, leading to possible errors in weak lensing results if left uncorrected.

## Acknowledgments

We would like to thank J. Peterson and E.-H. Peng for their help with PhoSim; M. Fisher-Levine, E. Sheldon, and T. Throwe for assistance with code and computing; and A. Plazas, P. O'Connor, and A. Rasmussen for useful comments and discussions. This work was supported by the Stony Brook University — BNL seed grant 37298-2-1103910.

## References

[1] LSST Science Book (2009), http://www.lsst.org/lsst/scibook.

[2] J. Peterson, *PhoSim: a code to simulate telescopes one photon at a time*, 2014 *JINST* **9** C04010.

[3] C.W. Walter, *The Brighter-Fatter and other sensor effects in CCD simulations for precision astronomy*, 2015 *JINST* **10** C05015, in *Precision Astronomy with Fully Depleted CCDs*, Brookhaven National Laboratory, U.S.A. 4–5 December 2014.

[4] S.E. Holland, C.J. Bebek, W.F. Kolbe and J.S. Lee, *Physics of Fully Depleted CCDs*, 2014 *JINST* **9** C03057 [arXiv:1403.6185].

[5] E. Bertin and S. Arnouts, *SExtractor: software for source extraction*, *Astron. Astrophys. Suppl. Ser.* **117** (1996) 393.

[6] A.A. Plazas, G.M. Bernstein and E.S. Sheldon, *Transverse electric fields' effects in the Dark Energy Camera CCDs*, 2014 *JINST* **9** C04001 [arXiv:1403.6127].

[7] A.A. Plazas, G.M. Bernstein and E.S. Sheldon, *On-sky measurements of the transverse electric fields' effects in the Dark Energy Camera CCDs*, *Publ. Astron. Soc. Pac.* **126** (2014) 750.

[8] SAOImage DS9 Reference Manual, http://ds9.si.edu/ref/.